Application of coupled bred vectors to seasonal-to-interannual forecasting and ocean data assimilation

Shu-Chih Yang[1,2,3], Christian Keppenne[1,4], Michele Rienecker[1] and Eugenia Kalnay[3]

[1] Global Modeling and Assimilation Office, NASA/GSFC

[2] Earth System Science Interdisciplinary Center, University of Maryland

[3] Department of Atmospheric and Oceanic Science, University of Maryland

[4] SAIC, inc.

Corresponding author:
Shu-Chih Yang
Department of Atmospheric Sciences,
National Central University,
Jhung-li, Taiwan 320
shuchih.yang@nasa.gov

September 2008
Submitted to Journal of Climate

Abstract

Coupled bred vectors (BVs), generated from the NASA/GMAO coupled general circulation model, are designed to capture the uncertainties related to slowly varying coupled instabilities. Two applications of the BVs are investigated in this study.

First, the coupled BVs are used as initial perturbations for ensemble forecasting purposes. Results show that the seasonal-to-interannual variability forecast skill can be improved when the oceanic and atmospheric perturbations are initialized with coupled BVs. The impact is particularly significant when the forecasts are initialized from the cold phase of tropical Pacific SST (e.g. August and November) because at these times the early coupled model errors, not accounted for in the BVs, are small.

Second, the structure of the BVs is applied to construct hybrid background-error covariances carrying flow-dependent information for the ocean data assimilation. Results show that the accuracy of the ocean analyses is improved when Gaussian background covariances are supplemented with a term obtained from the BVs. The improvement is especially noticeable for the salinity field.

1 Introduction

Seasonal-to-interannual predictions (SIPs) with coupled general circulation models (CGCMs) are carried out with ensemble forecasts in order to capture the uncertainties related to coupled instabilities, mainly associated with the El Nino-Southern Oscillation (ENSO) phenomenon. There are various ways to generate the ensemble perturbations. For example, in the NASA Global Modeling and Assimilation Office (GMAO) CGCM, the atmospheric and oceanic initial conditions are currently perturbed independently. The oceanic/atmospheric perturbations are generated by taking the differences between randomly chosen snapshots. Because they are generated separately, the atmospheric and oceanic perturbations do not represent uncertainties associated with air-sea interactions. The NCEP Environmental Modeling Center's[*] lagged average forecast (LAF) procedure is another example. There, only the atmospheric initial conditions are perturbed. Besides the fact that the initial perturbations do not include error growth related to coupled instabilities, the ensemble initial conditions are not centered at the initial time. Thus, an unnecessary forecast-error source is introduced in the ensemble forecasts (Peña 2007, personal communication).

The breeding method (Toth and Kalnay 1993, 1997), a non-linear method to generate the initial ensemble perturbations, has been widely used in numerical weather prediction. The idea is extended to perform the breeding in a coupled dynamic system by taking advantage of the fact that errors of different temporal scales are characterized by different rates of saturation (Peña and Kalnay 2004). Coupled breeding is designed to isolate the

---

[*] The initial conditions of the atmosphere are taken from the forecasts of the global forecast system (for numerical weather prediction) at different lead times.

slowly-varying, coupled instabilities from the other instabilities present in a dynamical, coupled system. Studies show that such coupled instabilities can be identified with coupled bred vectors (BVs) when physically meaningful breeding parameters, such as the rescaling amplitude and rescaling period, are chosen (Cai et al. 2003, Peña and Kalnay 2004 and Yang et al. 2006a, 2007). Breeding experiments conducted under a perfect model scenario with the NASA/GMAO CGCM have shown that BVs have coupled properties related to the background ENSO variations (Yang et al. 2006a). Also, coupled BVs obtained from the operational CGCM, in which observations are assimilated into the model's ocean component, have many similarities with the one-month forecast errors (Yang et al. 2007). These results indicate the potential usefulness of coupled BVs for ensemble forecasting in CGCMs. The BVs make the projection of the ensemble perturbations onto the subspace of the coupled instabilities more likely. In this study, four pairs of coupled BVs are applied to the NASA/GMAO CGCM as initial ensemble forecasting perturbations, and the performance of the resulting ensemble predictions is compared to that of predictions initialized from the non-perturbed ocean analysis.

The structures of BVs are also incorporated within the framework of the oceanic data assimilation to explore a possible shortcut of coupled data assimilation, focused on the seasonal time scale. Studies by Corazza et al. (2002) and Yang et al. (2006b) suggest that the BVs, which represent the structures of day-to-day dynamical errors ("errors of the day"), can be used to augment the background error covariances in the data assimilation. These studies modify the error covariances to include the flow-dependent errors carried by the BVs. The resulting corrections to the background state are superior to corrections obtained with a state-independent, isotropic, background error covariance model as used in 3DVar or in optimal interpolation schemes. The concept of combining two types of background error covariances is known as hybrid data assimilation (Hamill and Snyder 2000). Several studies have explored the skill of hybrid ensemble assimilation schemes. Using ensemble perturbations derived from an Ensemble transform Kalman filter, Etherton and Bishop (2004) show that hybrid data assimilation has advantages over an optimal perturbation scheme. Another example is found in Wang et al. (2007a) where the background error covariances are augmented with ensemble perturbations provided by the Ensemble Transform Kalman Filter (ETKF). That work shows that improvements can still be obtained with as few as 5 ensemble members, despite the fact that a larger ensemble is necessary to avoid filter divergence in the (non-hybrid) EnSRF. These studies suggest that hybrid data assimilation is a feasible way to upgrade a data assimilation scheme that uses state-independent error statistics into a more advanced scheme that knows about the state-dependent error structures. In addition, Wang et al. (2007b) show that hybrid background-error covariances can be used in a variational framework (e.g. 3DVar) by including an additional penalty term in the cost function. Beck and Ehrendorfer (2005) also demonstrate that flow-dependent covariances can be applied to improve the performance of a 4DVar system. In their work, the flow-dependent covariances are constructed with a large number of singular vectors derived from a reduced-rank Kalman filter. It is also worth noting that in addition to the hybrid data assimilation some flow-dependent dynamic effects can be included by simple parameterizations of the background-error variances to be dependent on the vertical gradients of the background temperature (Behring et al. 1998, Weaver et al., 2003, 2005).

Our goal is to understand how coupled BVs representing “the errors of the month” can be used in a coupled system. A longer term goal is to perform completely coupled data assimilation in which each component in the coupled system (e.g. the atmosphere, the ocean and the land component) is updated to be as close to the nature as possible, in order to obtain balanced initial conditions for coupled forecasting. However, this may not be easy due to the very different types of growing errors in each model component. The coupled BV is a multi-variate structure in a dynamically balanced coupled state and so can be used to indicate the errors induced by coupled instabilities errors, which may not be corrected by an uncoupled background error covariance characterized by uncoupled instabilities (e.g. the synoptic weather scale in the atmospheric component). Thus, the coupled BVs could provide a simple way to take into account the coupled uncertainties. In this study, the oceanic component of the coupled BVs is used to augment the background error covariances in the ocean data assimilation (Section 4).

The paper is organized as follows. Section 2 contains a brief discussion of breeding in the NASA/GMAO CGCM. The performance of the ensemble forecasts is discussed in Section 3. Section 4 describes the hybrid ocean data assimilation scheme and results from several assimilation experiments are compared in Section 5. Section 6 contains a summary and discussion.

2. Coupled Breeding in the NASA GMAO coupled GCM

2.1. The coupled GCM

The NASA GMAO coupled CGCM is a fully coupled global ocean-atmosphere-land system. It is comprised of the NASA Seasonal-to-Interannual Prediction Project's Atmospheric General Circulation Model (NSIPP-AGCM) described in Bacmeister et al. (2000), the Poseidon OGCM (Schopf and Loughe 1995, Yang et al. 1999), and the Mosaic land surface model (LSM, Koster and Suarez 1992).

The NSIPP-AGCM is run at a 2.5° zonal by 2° meridional horizontal resolution and 34 unequally spaced sigma layers with high resolution (<200m) in the lower 2 km of the atmosphere. Its prognostic variables are wind, temperature, specific humidity and surface pressure. The Poseidon OGCM is a reduced gravity isopycnal model. It is run at a 5/8° zonal by 1/3°meridional horizontal resolution with 27 vertical layers. Its prognostic variables are layer thickness, zonal and meridional current, temperature and salinity. Implementation details of the coupled system are provided in Vintzileos et al. (2003). The atmosphere and ocean states are coupled daily without flux correction.

In the operational configuration, 12-month ensemble forecasts are initialized on the 1st day of every month from an ensemble of initial conditions. The oceanic initial conditions are generated by perturbing the analysis fields obtained from the optimal Interpolation (OI) assimilation (Sun et al., 2007) that assimilates temperature observations. The atmospheric initial conditions are generated by perturbing the state of the NSIPP AGCM forced with observed sea surface temperatures (SSTs). The current retrospective ensemble prediction system has six ensemble members with three ocean-only perturbations and two atmosphere-only perturbations in addition to the original ocean-atmosphere initial conditions.

The coupled breeding experiments are conducted with oceanic OI analyses assimilating temperature and salinity observations. The impact of using the bred perturbations to initialize the ensemble forecasts is investigated by comparing with the GMAO operational ensemble system.

2.2. Coupled breeding experiments

A two-sided coupled breeding cycle is performed from January 1993 to December 2006, with the initial conditions discussed above. The procedure is similar to Yang et al. (2006a, 2007). The rescaling period is chosen to be one month to isolate the slowly varying coupled ENSO-related instabilities. The coupled BVs then represent "the errors of the month".

The coupled BVs are calculated every month by rescaling the difference between the one-month positive and negative perturbed coupled forecasts at the end of the month:

$$b_{i+1} = r[M(x_i + b_i) - M(x_i - b_i)] = r\widetilde{b}_{i+1} \qquad (2.1)$$

$$r = \sqrt{\frac{< b_i, \mathbf{A} b_i >}{< \tilde{b}_{i+1}, \mathbf{A} \tilde{b}_{i+1} >}}\,. \qquad (2.2)$$

In Eq (2.1), b_i is the rescaled coupled BV at month i, $\widetilde{b}_{i+1}$ is the non-rescaled vector at month (i+1), M represents the one-month nonlinear integration carried out by the CGCM and r is the rescaling factor (i.e., the inverse of the monthly growth). The bred perturbation is rescaled according to the growth of the chosen rescaling norm $S_A = \sqrt{< b_i, \mathbf{A} b_i >}$ (see below) and then added and subtracted from the initial coupled state of the next breeding cycle for the two-sided breeding. The chosen norm, $S_\mathbf{A}$, represents the initial amplitude that the perturbation should have after it has been rescaled. The chosen norm is defined with the operator **A** in Eq (2.2). **A** is individually defined for each rescaling norm.

Four rescaling norms and amplitudes are chosen:

BV1: The root mean square (RMS) of the BV SST in the Niño3 region (150°W-90°W, 5°S-5°N). This norm is rescaled to s_1=0.1°C

BV2: The RMS of the BV D20 (the depth of 20°C isotherm) in the central equatorial Pacific (150°E-190°E, 2.5°S-2.5°N) and the rescaling magnitude is s_2=1.5m.

BV3: The RMS of the perturbations associated to the first four long wave modes (Kelvin and three Rossby modes) according to the calculation of Boulanger and Menkes (1995). With u' and η' denoting the BV zonal current and surface height reconstructed from the first four wave modes, the RMS of the normalized $[u', \eta']$ in the tropical Pacific (130°E-80°W, 5°S-5°N) is rescaled to $s_3=6.5\times10^{-3}\mathrm{m}^2\mathrm{s}^{-1}$.

BV4: The RMS of the work done on the oceanic perturbations by the atmospheric perturbations (see Goddard and Philander 2000). The RMS of $\tau_x'\overline{u} + u'\overline{\tau}_x$ in the tropical Pacific (130°E-80°W, 5°S-5°N), where $\overline{u}$ and $\overline{\tau}_x$ are the climatology of the zonal current and zonal wind stress, u' and τ_x' are the BV zonal current and wind stress, is rescaled to $s_4=0.1\mathrm{Nm}^{-1}\mathrm{s}^{-1}$.

BV2 and BV3 represent growing errors associated with upper ocean dynamics while BV1 and BV4 are related to coupling processes at the atmosphere-ocean interface.

Figure 1 shows four rotated EOF modes based on the subspace of the first 6 EOFs of the equatorial temperature from the 4 BVs, explaining 42% of the total variance. The EOFs are shown in the rotated space for illustration to minimize differences related to small scales that are associated with the orthogonality requirement of the EOFs and to indicate the locations of the growing signals. By doing so, the dominant modes are rotated to separate the large variances near the surface of the eastern boundary. In addition, these modes are arranged in the figure according to the longitudinal location of the dominant structures instead of the explained variances in order to demonstrate the propagating modes in the subsurface.

Our results show that equatorial subsurface temperatures from the four pairs of BVs generally have similar dominant structures: large variances are ranging from the subsurface of the western-central Pacific and to the surface of the eastern Pacific. There are also differences in details associated with the rescaling norms: for example, BV1, BV2, and BV4 have clearer variability associated with surface processes near the eastern boundary (about 24% of the total variance) but this process is less dominant in the BV3 (15.5% of the total variance).

Note that while the fully coupled BVs are used to initialize the ensemble forecasts in this study (Sections 4), only the oceanic bred-perturbations are applied in the data assimilation (Sections 4 and 5), and that the rotated EOFs (Figure 1) are shown to describe the general characteristics of the BVs, but the individual monthly fields are used in the applications.

3. Results from coupled ensemble forecasting

Following Section 2.2, four pairs of two-sided BVs (±BVs) are applied as the initial ensemble perturbations and 12-month ensemble forecasts are carried out for February, May, August and November initial conditions from 1993 to 2005. The BV perturbations are applied only to the initial condition at *t*=0, the normal procedure for initialization in ensemble forecasting. The control forecasts for comparison are the forecasts initialized with the unperturbed initial conditions as discussed in section 2.1 (i.e., the OI ocean analysis and the atmospheric restarts from integrations with specified SSTs).

The GMAO CGCM has skill for predicting interannual variabilities (http://gmao.gsfc.nasa.gov/cgi-bin/products/climateforecasts/index.cgi). Shown as an example, Figure 2 is the forecast Niño3 index starting from the November initial conditions perturbed with four pairs of BVs and compared with the control forecast and with the observed Niño3 index, represented by the Reynolds SST anomaly. The forecast anomalies are calculated relative to the forecast climatology to remove the coupled model drift. The control forecast and BV ensemble forecasts have predicted similar SST variations at early forecast lead-time but some BV ensemble members (and therefore the BV ensemble mean) often achieve a better forecast skill than the control at longer lead-times (e.g., the forecasts started from November 1995, 1998, 2000, and especially 2005).

Considering that the ensemble averaging may benefit the forecast skill, the impact of using the bred perturbations is assessed by comparisons with the operational ensemble forecasts with the GMAO CGCM, in which the initial atmospheric and oceanic perturbations are prepared separately and thus uncoupled (Sec 2.1). We should note that the BV and operational ensemble systems are initially centered on different oceanic analyses, and thus their forecast skills will depend on the quality of the oceanic analyses and they cannot be compared directly. Therefore, the impact is investigated by comparing the improvements of the ensemble mean against its own control (unperturbed initial condition) forecast.

Figure 3 shows the reduction in RMS errors from the ensemble mean using the BVs ensemble and the operational ensemble in the tropical eastern Pacific (150ºE-90ºE, 15ºS-15ºN). The reduction is defined as the difference between the SST RMS errors from the ensemble mean and from the control (unperturbed initial conditions) forecasts. This quality also indicates how much additional skills could be gained by the use of the ensemble. Overall, the BV ensemble has a larger impact on the control forecast than the operational ensemble. Except for May initial condition, the advantage from BV ensemble increases as the forecast period lengthens. We note that the effect of the spring barrier in the control forecast (not shown) is evident with the sudden increase of the error growth for forecasts after the spring season. The BV ensemble is able to reduce this rapid growth error growth and thus alleviate the sudden loss of prediction skill. The benefit from BV ensemble at long lead-times is especially significant in August and November initial conditions, compared to the operational ensemble.

For the cases with May initial conditions, the errors are large and grow fast early in both forecasts. This is because the forecast errors of those cases have larger uncertainties in addition to the initial errors, with the influence of large systematic model errors. When targeting the late spring to early summer time, the model climatology has a mean thermocline that is too deep in the eastern Pacific, limiting the prediction skill for SST. Even so, the BV ensemble suggests a larger positive impact on predicting the SST anomaly during the boreal spring and summer seasons than the operational ensemble.

The impact is further examined in the spatial patterns of forecast SST anomalies at a lead-time of 9 months. Figure 4 shows the spatial pattern correlation between the observed SST anomaly and the forecast SST anomaly at a 9-month lead for May and November initial conditions. The results from the ensembles (left panels) are compared with the control forecast (middle panels). Their differences (right panels) indicate whether additional skill is gained from the ensemble. The first and third rows in Figure 4 are the results related to BV ensemble and the second the forth rows are the results related to the operational ensemble. Overall, the bred perturbed ensemble forecasts is able to provide positive impact in the equatorial and southeast Pacific regions while the impact becomes less evident with the operational ensemble. The skill of the ensemble forecasts from May initial conditions are more comparable to the control forecast with either BV or operational ensemble perturbations. As discussed above, the boreal spring initial conditions may limit the skill because of the rapid growth of model errors at early lead-times. However, even in those cases, the bred perturbations exhibit improvements in the SST structures outside the cold tongue region, mitigating the negative correlation patterns in the control forecasts (shown in the south of the Pacific in Figures 4c and 4f). Despite the fact that the control for the operational system is slightly better than the control used for the BVs for May, the operational ensemble degrades the forecast slightly, whereas for the BV ensemble improves the forecast more. Therefore, one might expect to get a similar improvement if the BV ensemble was used with the operational ensemble.

The advantage from the BVs over the operational ensemble is significant for November initial condition. From Figure 4i, the improvement along the equatorial region implies that the ensemble predictions with the coupled BV structures are able to capture the probable displacements of the thermocline along an extensive region of the equatorial Pacific. However, we note that the BV ensemble does bring more negative impact than the operational ensemble in the region north of the warm waters of the Western equatorial Pacific (Figure 4c and 4i). This may be associated with the fact that the coupled BVs are designed to capture the coupled uncertainties related to ENSO variability and focus entirely on the equatorial waveguide.

The results shown in Figures 3 and 4 suggest that allowing the initial ensemble perturbations to be naturally coupled can provide a greater advantage than uncoupled perturbations for improving the ensemble forecast skill on seasonal-to-interannual timescales. Given the seasonality of the cold tongue development, results suggest that the benefit from using the BV ensemble perturbations is large especially when the forecasts are initialized from the cold phase of the tropical Pacific SST season. During the warm phase (e.g. May), the coupling strength in the eastern Pacific is smaller. The forecast skill benefits less from the coupled BV perturbations, and instead is more closely related to the skill in predicting the mean structure (the model climatology).

4. Ensemble-based hybrid ocean data assimilation

The hybrid assimilation combines the stability of a flow-independent error-covariance model with the adaptive properties of a flow-dependent model. Following Hamill and Snyder (2000), the background error covariance matrix ($\mathbf{P}_b$ in Eq (4.1)) in the hybrid data assimilation is the combination of the background error statistics from two sources, indicated as $\mathbf{P}_b^0$ and $\mathbf{P}_b'$ in Eq (4.1), with the weighting coefficient α ranging between 0 and 1.

$$\mathbf{P}_b = (1-\alpha)\mathbf{P}_b^0 + \alpha\mathbf{P}_b'. \tag{4.1}$$

In Eq (4.1), $\mathbf{P}_b^0$ contains the flow-independent error covariance estimates and $\mathbf{P}_b'$ is the flow-dependent term. Ensemble perturbations have been used to form $\mathbf{P}_b'$ in several recent studies (Etherton and Bishop, 2004; Wang et al., 2007a,b) as discussed in the introduction. Yang et al. (2006b) use the BVs to construct $\mathbf{P}_b'$ and show that the resulting hybrid data assimilation is more accurate than a 3DVar analysis.

Following Yang et al. (2006b), we use the BVs to augment the background error covariance of an optimal interpolation scheme. The $\mathbf{P}_b'$ term is formed as shown in Eq (4.2), where $\mathbf{b}$ is an ensemble-associated matrix with four columns corresponding to four BVs. Since BVs provide only the structures and not the background amplitude, the factor s[*] in Eq (4.2) is used to rescale the variance amplitude so that the trace of $\mathbf{P}_b'$ is the same as that of $\mathbf{P}_b^0$ (according to the amplitude of the background error listed in Table 1):

$$\mathbf{P}_b' = s\mathbf{b}\mathbf{b}^T = \hat{\mathbf{b}}\hat{\mathbf{b}}^T . \tag{4.2}$$

We should note that while $\mathbf{P}_b^0$ is chosen for specific scales and is constant over the assimilation experiments, ***b*** is derived from a monthly coupled breeding cycle (Eqs 2.1 and 2.2).

An optimal weighting in Eq (4.1) was experimentally found to be $\alpha \approx 0.3$. The optimality of α was assessed by evaluating the size of the innovations (observation minus forecast) over a 1-month assimilation cycle. With $\alpha = 0$, the scheme reverts to optimal interpolation. A similar number ($\alpha = 0.4$) is suggested by Wang et al. (2007a) with a hybrid OI assimilation to take into account the contributions from the ensemble-based covariance. Moreover, it is the ensemble structures that matter in our implementation,

---

[*] Note that the factor, s, is associated with the background error variance and is different from (2.1), in which s_A is used as the rescaling amplitude to generate coupled BVs.

since we have rescaled the variance amplitude corresponding to the ensemble-based covariance (4.2).

The analysis applies the Kalman filter update equation,

$$x_a = x_b + \mathbf{K}[y - H(x_b)] = x_b + \mathbf{P}_b\mathbf{H}^T[\mathbf{HP}_b\mathbf{H}^T + \mathbf{R}]^{-1}[y - H(x_b)]. \qquad (4.3)$$

Here **K** is the Kalman gain, **R** is the observation-error covariance matrix, x_a is the analysis, x_b is the background state and y is the observation vector (including temperature from TAO and PIRATA moorings, and XBTs, and temperature and salinity from Argo drifters). The H operator in this application is a tri-quadratic interpolation operator that interpolates the appropriate field of the model state vector to the location of each observation. **H** is the matrix of these mappings from model space to observation space. We note that the observations are not necessarily required to directly observe the analysis at the grid point; however, the observations must correspond to state-vector variables.

The implementation follows Keppenne and Rienecker (2003). The square root, $\mathbf{Q} = \mathbf{H}\hat{\mathbf{b}}$, of $\mathbf{HP}_b'\mathbf{H}^T$ (the background error covariance in the observation space), is used rather than $\mathbf{P}_b'$. The Kalman gain is reformulated as:

$$\begin{aligned}\mathbf{K} &= [(1-\alpha)\mathbf{P}_b^0 + \alpha(\mathbf{C}\bullet\mathbf{P}_b')]\mathbf{H}^T\{\mathbf{H}[(1-\alpha)\mathbf{P}_b^0 + \alpha(\mathbf{C}\bullet\mathbf{P}_b')]\mathbf{H}^T + \mathbf{R}\}^{-1} \\ &= (1-\alpha)\mathbf{P}_b^0\mathbf{H}^T[(1-\alpha)\mathbf{HP}_b^0\mathbf{H}^T + \alpha\mathbf{C}\bullet\mathbf{QQ}^T + \mathbf{R}]^{-1} \\ &\quad + \alpha(\mathbf{C}\bullet\hat{\mathbf{b}}\mathbf{Q}^\mathbf{T})[(1-\alpha)\mathbf{HP}_b^0\mathbf{H}^T + \alpha\mathbf{C}\bullet\mathbf{QQ}^T + \mathbf{R}]^{-1},\end{aligned} \qquad (4.4)$$

where the Schur (element by element) product, $\mathbf{C} \bullet \mathbf{Q}\mathbf{Q}^T$, of $\mathbf{Q}\mathbf{Q}^T$ with a compactly supported correlation matrix, **C,** is applied to remove spurious long-range covariances from the Kalman gain (e.g., Houtekamer and Mitchell, 2001). The assimilation is distributed and each processor applies a different regional analysis (see Keppenne and Rienecker, 2003). After replacing Eq (4.4) in Eq (4.3), the vector, $\mathbf{a} = [(1-\alpha)\mathbf{H}\mathbf{P}_b^0\mathbf{H}^T + \alpha\mathbf{C} \bullet \mathbf{Q}\mathbf{Q}^T + \mathbf{R}]^{-1}[\mathbf{y} - H(\mathbf{x}_b)]$), which has the size of the observation vector, is computed first. The analysis at grid point *i* is then obtained as:

$$\mathbf{x}_i^a = \mathbf{x}_i^b + (1-\alpha)\mathbf{g}_i^T\mathbf{a} + \alpha\sum_{k=1}^{\mathbf{K}} \hat{\mathbf{b}}_{i,k}\mathbf{q}_k^T(c^i \bullet \mathbf{a}) \ . \tag{4.5}$$

In Equation (4.5), **g** is a vector of Gaussian correlations between grid point *i* and each observation location, $\hat{\mathbf{b}}_{i,k}$ is the *k*-th rescaled BV at grid point *i* and $\mathbf{q}_k$ is the *k*-th column vector of **Q**. As in Eq (4.4), a vector of correlation coefficients, c^i depending on the distance between grid *i* and each observation, is applied in order to localize the BV-associated term. The correlation function takes the form of Equation 4.10 in Gaspari and Cohn (1995). We note that the elements of the matrix **C** in Eq (4.4) are obtained similarly, but are functions of coordinate differences between pairs of observations. The BVs are also smoothed with a Gaussian filter before being used in Eq (4.4-5) to reduce small-scale noise associated with the small ensemble. Keppenne et al. (2008) have discussed that by doing so the covariances used in the analysis procedure will more closely correspond to those one would obtain from a much larger ensemble.

In this test, temperature and salinity observations are assimilated sequentially every 4 days during the year 2006 as summarized in Tables 1 and 2. Table 1 shows the amplitudes of the background and observation errors, and Table 2 the scales of the Gaussian function (**g** in Eq (4.5)), the correlation function (***C***) and the Gaussian filter applied to the BVs.

For comparison, a different ensemble set containing four time-independent ensemble perturbations are also used to augment $\mathbf{P}_b^0$. They are taken from the first 4 EOFs of differences derived from an ensemble of integrations similar to Borovikov et al. (2005) The first 4 EOFs explain 31% of the total global variance but locally more than 50% of the temperature variance in regions of the Pacific and Atlantic. The resulting hybrid background error covariances are multivariate but constant in time, as they do not track variations of the background flow.

In this study, the assimilation experiment that uses only the Gaussian-type background error covariance is referred to as the control run, the hybrid assimilation that uses 4 BVs is called the "4BV" run and the one that uses time-independent ensemble-derived 4 EOFs is referred to as the "4EOF" run. The control run in this study provides the baseline to evaluate the effect from the time-dependent or time-independent background error covariances. We note that it is still common (as done at NCEP and at ECMWF and in the control run of this study) to assume a univariate background error covariance and adjust the analysis corrections (increments) using the temperature-salinity relationship. We also note that for a univariate assimilation, the impact of error variances based on gradient information (correlation length) is less important than the ratio of the background error variance to the observational error variance. Both are impacted by vertical gradients of the underlying state.

5. Application to ocean data assimilation

5.1. Background error covariances

Figure 5 shows the temperature error covariance structure corresponding to a unit temperature innovation near the thermocline in the equatorial western Pacific, (156°E, Equator, 150 m) for the different error-covariance representations discussed in Section 3. The two BV-based error covariances (bottom two rows) are chosen for the same calendar month but two different years to demonstrate the dependence on the background flow, characterized by different Niño3 SST anomalies: May 2006 corresponds to the developing state of the warm event occurring at the end of 2006 and May 1998 corresponds to the cold event of 1998. Note that the decorrelation and filtering functions discussed in Section 3 have been applied to the ensemble-based error covariances shown here.

From Figure 5, it is clear that the ensemble-based covariance from the EOF and BV ensembles have shorter zonal and vertical scales than those we chose in the Gaussian covariance. Note that the covariances are scaled by the variance at the chosen point (indicated by the cross in the figure). Due to sampling, the maxima may not collocate with the point of interest. The error covariance based on four EOF modes has large horizontal scales at this location similar to the 4BV-based covariance in May 2006. The zonal cross-section of the 4EOF-based covariance reflects the orientation of the thermocline (zonal sloping along the equator). The BV-based structure in May 2006 suggests that the horizontal scales are wider than in May 1998 and extend deeper at this location. In contrast, the vertical covariance structure extends towards the surface in May 1998. Compared to the 4EOF-based covariance, the zonal slope along the equatorial cross-section in the May 2006 BV-based covariance is more consistent with thermocline changes expected to occur during warm events. In addition, the meridional cross-section shows that the May 2006 covariance structure tilts downward south of the equator. Similar variations in structure are found near the surface of the eastern equatorial Pacific, where the May 2006 covariance expands more broadly from the surface to below 100 m, while the May 1998 covariance is limited near the surface (figure not shown). Such differences reflect variations in the equatorial upper ocean at those times: the BVs in the subsurface western-equatorial Pacific are characterized by large-scale variations in May 2006 while the variations of the BVs in May 1998 are characterized by flat structures in the subsurface since most of the uncertainties are limited near the surface.

The salinity covariance structure shown in Figure 6 corresponds to 165°E, 4°S and the depth of 100m. This location is above the halocline (the large salinity gradient in the vertical), and near the western edge of the salty tongue extending from the southeast Pacific. Kessler et al. (1999) pointed out that the salinity variation at this location has an ENSO-related variability resulting from the equatorward expansion of this salty tongue in the western Pacific. Similar to the temperature covariance shown in Figure 5, the 4EOF-based covariance is characterized by a large-scale feature with large amplitude strongly influenced by the climatological structures. The 4BV-based salinity covariance shows more localized structures horizontally and vertically. The vertical structures suggest that vertical displacements due to instabilities are more detectable in the bred modes. For example, in May 2006, the positive-signed covariance pattern has a structure tilting from the subsurface of the western equatorial Pacific toward the surface near 170°E. This suggests that an assimilation increment related to the salty water subsurface can extend toward the surface similar to the structure of the background salinity. Given the sharp vertical gradient, the covariance structure has a significant negative pattern below 200m near the equator. In addition, another negative pattern near the surface in the western Pacific reflects the displacement of the warm, fresh water near the surface. In contrast, the features of the May 1998 covariance are more localized and shift closer toward the surface. The background salinity in May 1998 shows very fresh water near the surface of the equatorial Pacific, blocking the invasion of the salty water from the subsurface (figure not shown).

The ensemble-based background error covariances also provide multivariate covariances between temperature and salinity errors. Figure 7 shows the impact of one salinity observation at (165ºE, 4ºS 100m) on the temperature increments. The EOF-based covariance shows that the correlation is large-scale and relevant to the mean depth of the thermocline. In contrast, the BV-based covariance with different background conditions gives very different correlations. For May 2006, the salinity at this location is positively correlated with the temperature and the corresponding zonal and vertical scales are much larger than the 4EOF-based covariance. This suggests that the impact of the salinity observation on temperature corrections could be extended further in the zonal and vertical directions with covariances estimated for May 2006. However, the same positive innovation would have had a very different influence on the temperature in May 1998, when the corresponding covariance has shorter horizontal and vertical scales and the sigh is reversed from May 2006. In summary, these BV-based covariance structures reflect uncertainties associated with the background state evolution.

5.2 Results of the assimilation experiments

The covariance structures from 4EOF and 4BVs are now used to complement the Gaussian covariances of a simple optimal interpolation scheme and the impact on ocean analyses is assessed. Because the time-dependent BVs are generated every month, the 4BV hybrid assimilation is performed every 4 days by linearly interpolating between the relevant monthly 4BV structures (referred to as 4day-4BV).

The overall performance of the different assimilation experiments is first examined through the innovation vectors (the "observation minus forecast" values, hereafter referred to as OMF), which also provide an estimate of the forecast errors, assuming that the observation errors are small. The time series of the RMS temperature and salinity OMF are shown in Figure 8. The OMF from all the hybrid assimilations are smaller than those from the control, which uses just the Gaussian covariance structures, indicating their ability to reduce the forecast error. For the temperature assimilation, both hybrid systems give similar improvements, except at the end of the year, where the 4EOF assimilation indicates a smaller OMF. For salinity assimilation, the 4day-4BV assimilation has the smallest RMS OMF of all methods, suggesting that the accuracy of the assimilation has clearly benefited from using the time-evolving structures. Also from

Figure 8, the level of relative improvement from 4BV or 4EOF is more apparent in salinity than in temperature.

The impact of the hybrid assimilation on the salinity analyses is evaluated for the upper ocean above the thermocline (upper 150 m). For this purpose, the global OMF values derived from 68 assimilation cycles (from March 2006 to December 2006) are binned into 5°×5° boxes to create the map of the mean RMS OMF corresponding to each experiment. The first two months of assimilation are not used for the computation because of the spin-up evident in salinity in Figure 8. Figures 9 (a) and (b) show the global distributions of the difference between the mean RMS OMF of the control and 4BV runs, and between the control and 4EOF runs, respectively. Red shades indicate improvements with respect to the control, and blue shades indicate that the univariate control analysis was better than the hybrid. It is clear that using 4BV or 4EOF improved the salinity analysis over the control in all three ocean basins, particularly in the southwest Pacific, the tropical Atlantic and the northern Indian Oceans. The improvements from using the 4BV are more extensive than for the 4EOF over all three ocean basins. The regions where the salinity assimilation was degraded by the hybrid assimilation are also broader in 4EOF than in 4BV, such as in the north Pacific near the date line and in the Indian Ocean Throughflow, indicating that bad corrections are imposed by the 4EOF covariance at those locations.

To verify the impact of the hybrid systems with independent data, the T-S relationships from monthly-averaged analyses are examined by regions mentioned above and are compared with those inferred from available CTD (Conductivity Temperature and Depth) temperature and salinity observations which have not been assimilated (Figure 10). In the southwest equatorial Pacific (Figure 10a), all the analyses (colored dots) show generally good agreement with the CTD T-S data, confirming that all the assimilations are successfully using the Argo observations. However, the control analysis includes water that is too fresh near the surface and too salty above the thermocline (near the 24.5 kg m^{-3} σ_θ surface) when compared with the CTD data (black dots). In 4BV, the T-S analysis indicates a closer relationship with the observed value near the surface and in the thermocline indicating a more accurate salinity maximum and that the vertical gradient is improved. The absence of the very fresh surface water in the 4BV analysis is the result of using the ARGO data (exhibiting a very good agreement with the ARGO T-S relationship, figure not shown). The broader T-S relationship from the 4EOF analysis compared with the CTD T-S relationship (or the control T-S) indicates that the corrections made with the 4EOF covariance structure do not extract the observation information well from the mixed layer to the thermocline. This analysis also introduces a broader range of subsurface T-S values near the 26.0-26.5 kg m^{-3} sigma levels. The time evolution of the corrections near the thermocline is discussed in section 5.2.1.

In the north-tropical Atlantic (Figure 10b), the control analysis does not represent well the observed structure while the 4BV and 4EOF analyses are closer to the observed data. However, the T-S relationships suggest that the improvement is primarily in the upper ocean with warmer, fresher water ($T > 20°C$ and $S < 36$ psu) than in the control. The improvement near the surface is better for the 4BV analyses than for the 4EOF analyses, which are missing the fresh surface values. In deeper waters the variability in the Atlantic is not well simulated by this model. However, the T-S relation is tighter in the 4BV analyses than in the 4EOF analyses. In spite of this, the mean temperature and salinity along the equator from the 4EOF analyses have better gradient structures (figure not shown). This also reflects the fact that the BVs are designed to capture error growth associated with the ENSO instabilities in the Pacific and thus the error growth in the Atlantic, though naturally captured as well, may be underestimated due to error saturation.

In the southeastern tropical Indian Ocean, the salinity and temperature variations in the upper ocean are strongly influenced by the Indonesian Throughflow and the precipitation patterns are influenced by Pacific ENSO events (Perigaud et al., 2003 and Murtugudde and Busalacchi, 1998). From Figure 10c, it is clear that the control analysis does not represent the T-S relationship as well as 4BV, as it is missing the salty water near the bottom of the thermocline (near the 23.0 kg m^{-3} σ_θ surface). However, the mass of Indonesian upper water is well described in the 4BV analysis, in good agreement with the observed CTD T-S relationship. In contrast, the 4EOF analysis is less effective at this location and introduces inappropriate water masses. This deficiency is associated with the low explained variance of the EOFs at this location (figure not shown).

These results demonstrate that the augmented covariances used in the hybrid assimilation result in a better use of the available observations.

5.2.1 Analysis on isopycnal surfaces

Figure 11 compares the three analyses with Argo salinity in terms of their evolution from March to July 2006 on the constant 24.5kg m^{-3} density surface in the upper thermocline. Note that the interpolation of the ARGO salinity to the model grid introduces some noisiness. Overall, all the salinity fields exhibit similar features in terms of the large-scale meridional and zonal gradients. However, there are differences in the details, particularly in the meridional salinity gradients and in the salty intrusion across the eastern equatorial region during May and June. The meridional gradient at the equator appears to be too strong in the control and in the 4EOF analyses, with (for example) fresher water just north of the equator near the dateline leading to a stronger meridional gradient there compared with the Argo and 4BV analyses. From May to July, the meridional gradient just south of the equator at 150°W is weaker in the control and the 4EOF than in the Argo data and in the 4BV analyses. In addition, the variations in the eastern Pacific, with fresh water from the north intruding across to the south in March and then salty water intruding from the south in May and June, are better represented in the 4BV analyses. These features are visible in Argo data, although they are somewhat smoothed out due to the distribution of the observations. The small-scale (eddy) activities in the 4BV salinity analyses suggest that the development of local instabilities is captured by the BV structures.

Twelve-months Hovmöller diagrams for the meridional cross section at 93.5°W (Figure 12) show that the salty water invasion present in the Argo data started in April, quickly crossed the equator in two months, and then retreated gradually. This feature corresponded to an anomalous, warm flow. Although all salinity analyses show the salty intrusion across the equator, the 4BV case better models the evolution of the retreat of the fresh intrusion and evolution south of the equator than the other analyses. However, the salty intrusion in the 4BV analyses crossing the equator is stronger and longer lasting than in the observations. The difference from the Argo time series could represent a sampling problem in the Argo data since salinity as high as 35.2 is evident north of the equator at about 95°W in May and 115°W in June (Figure 11). The results imply better-represented salinity structures feed back on the current structures and improve the advection processes through dynamical adjustment.

6. Summary and discussion

In this study, we investigate the potential applications of bred vectors generated from the NASA/GMAO coupled GCM and aim to capture the uncertainties related to the slowly varying coupled instabilities (ENSO variability). Two ways of using BVs to improve forecasts have been investigated, namely (1) their use as initial ensemble-forecast perturbations and (2) their use to construct hybrid background error covariances that carry the flow-dependent forecast error statistics for the oceanic assimilation procedure.

All four pairs of BVs generated with different norms show the dominance of growing errors near the thermocline but they also show specific characteristics associated with the different rescaling norms. The impact using these coupled bred perturbations for ensemble forecasting is evaluated by comparing with the operational ensemble prediction system, whose atmospheric and oceanic perturbations are uncoupled and independently perturbed. The comparisons are based on the improvements of the ensemble mean against its own control (unperturbed initial condition) forecast for a 13-year period.

The BV ensemble is able to reduce the mean RMS of forecast SST anomalous error in the tropical Pacific region for February, May, August and November initial conditions. The advantage of BV ensemble over the operational ensemble increases as the forecast period lengthens, except for May for which they become similar. The BV ensemble mitigates the loss of skill associated with the spring barrier, especially in August and November initial conditions, and shows valuable information after overcoming the spring barrier at long lead-time. For May initial conditions, the beneficial effect of using either type of ensemble is more limited because the large model seasonal drift (systematic error) complicates the error growth during the late-spring to summer season, and the forecast skill is more closely related to the skill in predicting the mean structure (the model climatology).

At a lead-time of 9 months, the BV ensemble exhibits positive impact on predicting phase of the SST anomalies, in contrast to the less clear impact from the operational ensemble system. The significant improvement is found in November initial condition and related to the displacements of the equatorial thermocline. Even for the difficult cases of May initial conditions, the BVs are able to reduce the loss of skill at the edge of the cold tongue. Therefore, we conclude that allowing the ensemble perturbations to be naturally coupled provides greater improvement to the forecast skill at seasonal-to-interannual timescales than the operational, non-coupled ensemble system.

The question of whether BVs represent the flow-dependent errors was further investigated with hybrid data assimilation experiments in which Gaussian background error covariances were augmented with a 4BV-based error covariance term. Assimilation results were compared with those obtained with flow-independent error covariance, including a Gaussian covariance and a hybrid covariance that augments the Gaussian covariance with climatological covariances from four dominant EOF modes generated by ensemble simulations. The ensemble-based covariance (4BV or 4EOF) has the advantage of being multivariate. Table 3 summarizes the characteristics of different types of assimilation experiments in this study.

While the BVs represent “the errors of the month”, the dominant EOF modes represent the features of seasonally averaged error structures. The 4BV-based error covariance shows that the covariance indeed is sensitive to the background state characterized by different horizontal and vertical scales. The 4BV-based covariances in both temperature and salinity are able to reflect the flow variations in the upper ocean. The salinity covariance reflects more local variabilities, including the fresh water near the surface and the changes near the halocline. For example, the zonal and vertical May decorrelation scales are wider during the development of the 2006 warm event than during early stages of the 1998 cold event. The cross-correlation between temperature and salinity is also sensitive to the background variations.

Assimilation results using data from 2006 indicate that the hybrid covariances improve the quality of the analyses for both the temperature and salinity fields. For temperatures, the 4EOF and 4BV-based covariances yield similar improvements upon the univariate analysis. For salinity, the hybrid BV system gives the best results. The positive impact over the control is particularly significant for salinity in the South Pacific, South Atlantic and Indian oceans where the T-S relationships for the hybrid BV system more closely resemble those of independent CTD observations. The results from the hybrid assimilations show that the salinity analyses are more accurate due to a better use of the Argo observations.

In the tropical Pacific, the improvement with the time-dependent BV structure results from a better vertical salinity gradient which reduces the near-surface fresh water in the western equatorial Pacific. More improvements are visible in the time evolution of the salinity analyses. The BV salinity analysis can better reproduce the initial stages of the fresh/salty water intrusion across the eastern equatorial Pacific and the evolving pattern is better captured than in the control or hybrid 4EOF salinity analyses. These results confirm that the analysis can be improved with the flow-dependent error statistics obtained from the 4BVs. With the 4EOF-based covariances, although the overall structure is also well represented in the analysis, the ability to have corrections associated with local instabilities is less clear. However, in the Atlantic, the temperature analysis improvement is greater with the EOF-based hybrid covariance than with the BV-based covariances. This is not surprising since the BVs were rescaled such as to capture the ENSO-related coupled instabilities in the Pacific.

We plan to investigate the use of the BVs in coupled forecasts in which the ocean is initialized from the hybrid assimilation. A similar hybrid system can also be used to improve the background error covariance used in an ocean Ensemble Kalman Filter (EnKF) by augmenting them with covariances derived from coupled BVs. Through the same hybrid form, this method can be used with a variational or other ensemble-based assimilation schemes for enhancing their background error covariance. The hybrid use of coupled BVs in a variational scheme is not different from the implementation here since the "errors of the month" information could be included directly in the specified background error covariances as in Yang et al. (2006b) or include a set of extended control variables associated with the ensemble-based error covariance in the cost function as in Wang et al. (2007b).

Note that in this study, only the oceanic component of the coupled BVs was used in the ocean data assimilation. The atmospheric component of the BVs could also be applied in a coupled data assimilation system to perturb the surface conditions and mimic uncertainties of surface (wind) forcing, which are also an important factor limiting ENSO-prediction skill.

Acknowledgements

The authors are very grateful for technical support from the NASA/GMAO staff. This research was supported by funding (WBS 802678.02.12) from NASA's Modeling, Analysis and Prediction (MAP) program. S-C Yang and E. Kalnay were also supported by NASA grant NNG06GB77G. Computational resources were provided by the NASA Center for Computational Sciences at the Goddard Space Flight Center.

References

Bacmeister, J., P. J. Pegion, S. D. Schubert, and M. J. Suarez, 2000: An atlas of seasonal means simulated by the NSIPP 1 atmospheric GCM. Vol. 17. NASA Tech. Memo. 104606, Goddard Space Flight Center, Greenbelt, MD, 194 pp.

Beck, A., and M. Ehrendorfer, 2005: Singular-vector-based covariance propagation in a quasi-geostrophic assimilation system. *Mon. Wea. Rev.*, **133**, 1295-1310.

Behringer, D., M. Ji, and A. Leetma, 1998: An improved coupled model for ENSO prediction and implications for ocean initialization. Part I: The ocean data assimilation system. *Mon. Wea. Rev.,* **126,** 1013–1021.

Borovikov, A. Y., Rienecker, M. and Keppenne, C. L. and Johnson, G. C., 2005: Multivariate error covariance estimates by Monte-Carlo simulation for assimilation studies in the Pacific Ocean, *Mon. Wea. Rev.*, **133**, 2310-2334.

Boulanger, J.-P., and C. Menkes, 1995: Propagation and reflection of long equatorial waves in the Pacific and reflection of long equatorial waves in the Pacific Ocean during 1991-1993 El Nino. *J. Geophys. Res.*, **100**, 25041-25059.

Cai M., E. Kalnay, and Z. Toth, 2003: Bred vectors of the Zebiak-Cane model and their application to ENSO predictions. *J. Climate*, **16**, 40-55.

Corazza, M., E. Kalnay, D. J. Patil, E. Ott, J. Yorke, I. Szunyogh, M. Cai, 2002: Use of the breeding technique in the estimation of the background error covariance matrix for a quasigeostrophic model. AMS Symposium on Observations, Data Assimilation and Probabilistic Prediction, Orlando, Florida, 154-157.

Etherton, B. J., and C. H. Bishop, 2004: Resilience of hybrid ensemble/3DVAR analysis schemes to model error and ensemble covariance error. *Mon. Wea. Rev.*, **132**, 1065-1080.

Gaspari, G. and Cohn, S., 1999: Construction of correlation functions in two and three dimensions. *Quart. J. Roy. Meteor. Soc.*, **125**, 723-757.

Goddard, L. and S. G. H. Philander (2000): The energetic of El Niño and La Niña. *J. Climate*, **13**, 1496-1516.

Hamill, T. M, and C. Snyder, 2000: A hybrid Ensemble Kalman Filter 3D Variational analysis scheme. *Mon. Rev. Rev.*, **128**, 2905-2919.

Houtekamer, P., and H. Mitchell, 2001: A sequential ensemble Kalman filter for atmospheric data assimilation. Mon. Wea. Rev., **129**, 123-137.

Keppenne, CL., and M. Rienecker, 2003: Assimilation of temperature into an isopycnal ocean general circulation model using a parallel ensemble Kalman filter. *J. Mar. Sys.*, **40-41**, 363-380.

-----------------, M.M. Rienecker, J.P. Jacob, and R. Kovach, 2008: Error Covariance Modeling in the GMAO Ocean Ensemble Kalman Filter. *Mon. Wea. Rev.*, **136**, 2964-2982.

Kessler W. S., 1998: Interannual variability of the subsurface high salinity tongue south of the equator at 165°E. *J. Phys. Oceanogr.*, **29**, 2038-2049.

Koster, R., and M. Suarez, 1992: Modeling the land surface boundary in climate models as a composite of independent vegetation stands. *J. Geophys. Res.*, **97**. 2697-2715.

Murtugudde, R., and A. Busalacchi, 1998: Salinity effects in a tropical ocean model, *J. Geophys. Res.*, **103**, 3283–3300.

Peña, M. and E. Kalnay, 2004: Separating fast and slow modes in coupled chaotic system. *Nonlinear Process. Geophys.*, 11, 319-327.

Perigaud, C., McCreary J. P., and Zhang Q. K., 2003: Impact of interannual rainfall anomalies on Indian Ocean salinity and temperature variability, *J. Geophys. Res.*, **108**, 3319-3335.

Schopf, P., and A. Loughe, 1995: A reduced-gravity isopycnal ocean model: hindcasts of El Niño. *Mon. Wea. Rev.*, **123**, 2839-2863.

Sun, C., M. M. Rienecker, A. Rosati, M. Harrison, A. Wittenberg, C. L. Keppenne, J. P. Jacob, and R. M. Kovach, 2007: Comparison and Sensitivity of ODASI Ocean Analyses in the Tropical Pacific. *Mon. Wea. Rev.*, **135**, 2242–2264.

Toth, Z. and E. Kalnay, 1993: Ensemble forecasting at NMC: the generation of perturbations. *Bull. Amer. Meteor. Soc.*, **74**, 2317-2330

----------- and E. Kalnay, 1997: Ensemble Forecasting at NCEP and the Breeding Method. Mon. Wea. Rev., 125, 3297–3319.

Vintzileos A., M. M. Rienecker, M. J. Suarez, S.K . Miller, P. J. Pegion, and Julio T. Bacmeister, 2003: Simulation of the El Niño – Southern Oscillation phenomenon with NASA's Seasonal-to-Interannual Prediction Project coupled general circulation model. *CLIVAR – Exchanges*, **8(4), 25-27.**

Wang, X., T. M. Hamill, J. S. Whitaker, and Craig H. Bishop, 2007a: A comparison of hybrid ensemble transform Kalman Filter-OI and ensemble square-root filter analysis scheme. *Mon. Wea. Rev.*, **135**, 1055-1076.

------------, and C. Snyder, and T. M. Hamill, 2007b: On the theoretical equivalence of differently proposed ensemble/3D-Var hybrid analysis schemes. *Mon. Wea. Rev.*, **135**, 222-227.

Weaver, A. T., C. Deltel, E. Machu, S. Ricci, N. Daget, 2005: A multivariate balance operator for variational ocean data assimilation. *Quart. J. Roy. Meteor. Soc.*, **131**, 3605-3625

-----------------, Vialard, J. and Anderson, D. L. T. 2003 Three- and four-dimensional variational assimilation with an ocean general circulation model of the tropical Pacific Ocean. Part 1: formulation, internal diagnostics and consistency checks. *Mon. Weather Rev.*, **131,** 1360–1378

Yang, S., K.M. Lau and P.S. Schopf, 1999: Sensitivity of the tropical Pacific Ocean to precipitation induced freshwater flux. *Clim. Dynam.*, **15**, 737-750.

Yang, S-C, E. Kalnay, M. Cai and M. Rienecker, 2007b: Bred vectors and forecast errors in the NASA coupled general circulation model. *Mon. Wea. Rev.*, **136**, 1305-1326.

-------------, M. Cai, E. Kalnay, M. Rienecker, G. Yuan and Z. Toth, 2006a: ENSO Bred Vectors in Coupled Ocean-Atmosphere General Circulation Models. *J. Climate*, **19**, 1422–1436.

-----------, M. Corazza, A. Carrassi, E. Kalnay, and T. Miyoshi, 2006b: Comparison of ensemble-based and variational-based data assimilation schemes in a quasi-geostrophic model, 10th Symposium on Integrated Observing and Assimilation

Systems for the Atmosphere, Oceans, and Land Surface, 2006 AMS meeting in Atlanta, GA.

Table Captions

Table 1 Amplitude of the background and observation errors

Table 2 Scales used in the assimilation experiments

Table 3 Summary of the characteristics of the assimilation experiments

Figure captions

Figure 1 Rotated EOF modes (scaled to unit variance) from four BVs in the subsurface of the equatorial Pacific. From the left to the right, rotated EOFs modes derived from the oceanic part of the BV1, BV2, BV3 and BV4.

Figure 2 Niño3 index anomaly forecast starting from November initial conditions showing the ensemble perturbed with 4 pairs of BVs (red lines) the control forecast initialized with the unperturbed initial condition (black line). Results are validated with the observed Niño3 index (the Reynolds SST), denoted as the dashed blue line. The forecast anomalies are calculated relative to the climatological forecast drift.

Figure 3 Differences in mean RMS error between the ensemble mean and the control forecasts with the BV and operational ensemble system for (a) February, (b) May, (c) August and (d) November initial conditions during the period of 1993 to 2005. The solid lines indicate the result from using the BV ensemble and the dashed lines for the operational ensemble. Mean RMS error is defined as the time-averaged RMS difference between the observed SST anomaly (Reynolds SST) and the forecast SST anomaly in the tropical central-eastern Pacific (180°-90°W, 15°S-15°N).

Figure 4 SST anomaly correlations with observations at the 9th-month lead time for mean ensemble-forecasts (left panels), unperturbed (control, middle panels) and the differences between the ensemble mean and unperturbed forecasts (right panels). (a)-(c) are for the BV ensemble system from May initial conditions. (d)-(f) are the same as (a)-(c) excpet for the operational ensemble system. (g)-(l) are the same as (a)-(c) expect from November initial conditions.

Figure 5 Temperature correlation structure associated with a hypothetical temperature observation at (156°E, Equator, 150m, denoted by ×) in the control (a Gaussian function, first row), the 4EOF-case (second row), the 4BV-case in May 2006 (third row) and the 4BV-case in May 1998 (fourth row). Horizontal, zonal and the meridional cross sections are shown from left to right, respectively.

Figure 6 Same as Figure 5 but for a salinity observation at (165°E, 4°S, 150m).

Figure 7 Temperature correlation structure associated with a hypothetical salinity observation at (165°E, 4°S, 100m, denoted by ×) in the 4EOF-case (first row), the 4BV-case in May 2006 (second row) and the 4BV-case in May 1998 (third row). Horizontal, zonal and the meridional cross sections are shown.

Figure 8 Time series of the global RMS of (a) the temperature OMF and (b) the salinity OMF.

Figure 9 Differences between the salinity RMS OMF above 150m of the control and of (a) the 4BV analyses and (b) the 4EOF analyses.

Figure 10 T-S-diagram from the analysis (colored dots) and the CTD data (black dots) in (a) the south western equatorial Pacific (162.5°E-167.5°E, 0°S-5°S), (b) the northern tropical Atlantic (2.5°W-2.5°E, 2°N-7°N) and (c) the south east tropical Indian Oceans (85°E-90°E, 4°S-9°S). Note that the contours are isolines of σ_θ.

Figure 11 Monthly-mean salinity on the 24.5 kg m^{-3} density surface from March 2006 to July 2006. From left to right are the Argo data, the control analysis, the 4BV analysis and the 4EOF analysis. Each map uses the same 30 days of Argo salinity, from March through July 2006.

Figure 12 Salinity variations along a meridional cross-section at 93.5°W during 2006 in (a) the ARGO data, (b) the control analysis, (c) the 4BV analysis, and (d) the 4EOF analysis.

Table 1 Amplitude of the background and observation errors

	Background	**Observation**			
		TAO	**XBT**	**ARGO**	**PIRATA**
T (°C)	0.7	0.5	0.5	0.5	0.5
S (psu)	0.07			0.01	

Table 2 Scales used in the assimilation experiments

	$\mathbf{P}_b^0$	$\mathbf{P}_b'$	
	Gaussian	**Localization**	**Filtering**
X	20°	8°	4°
Y	5°	4°	2°
Z	100m	100m	N/A

Table 3 Summary of the characteristics of the assimilation experiments

	CNT	4EOF	4day_4BV
Assimilation cycle	4 days		
Background error covariance	Univariate	Multivariate	Multivariate
Flow dependency	No	No	Yes Update every 4-day

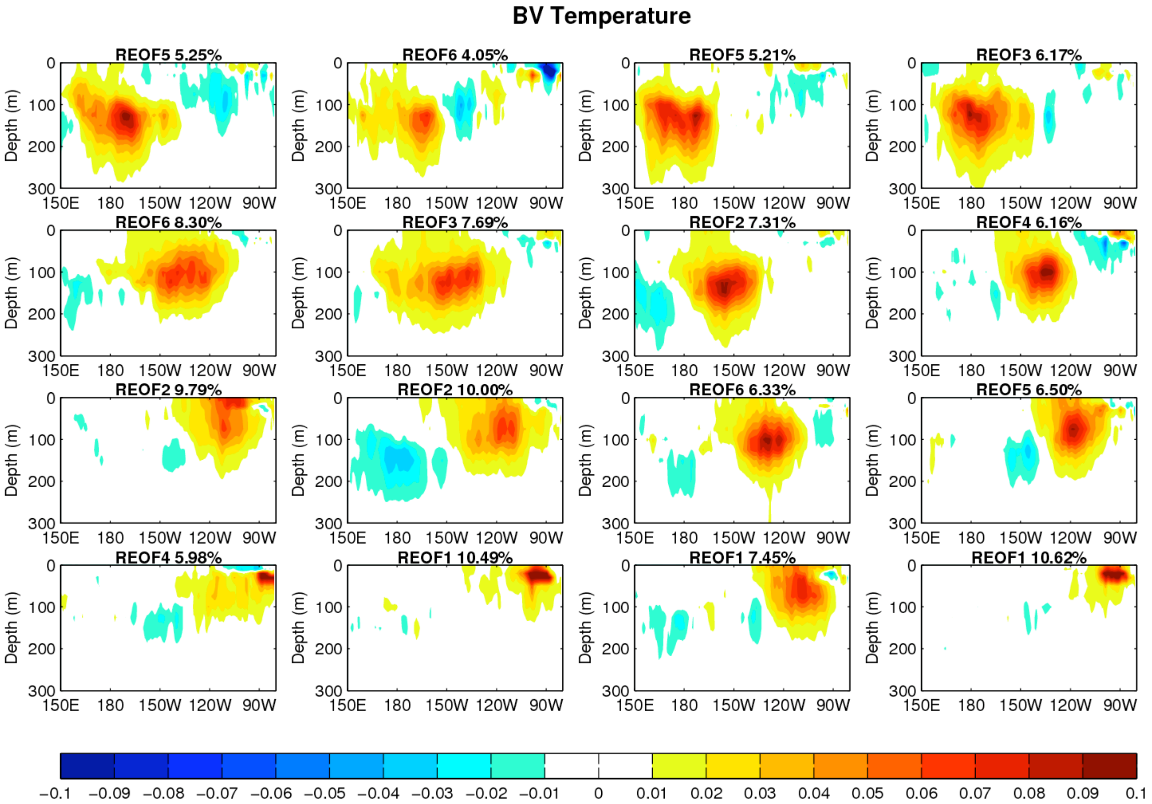

Figure 2 Rotated EOF modes (scaled to unit variance) from four BV temperature in the subsurface of the equatorial Pacific. From the left to the right, rotated EOFs modes derived from the oceanic part of the BV1, BV2, BV3 and BV4.

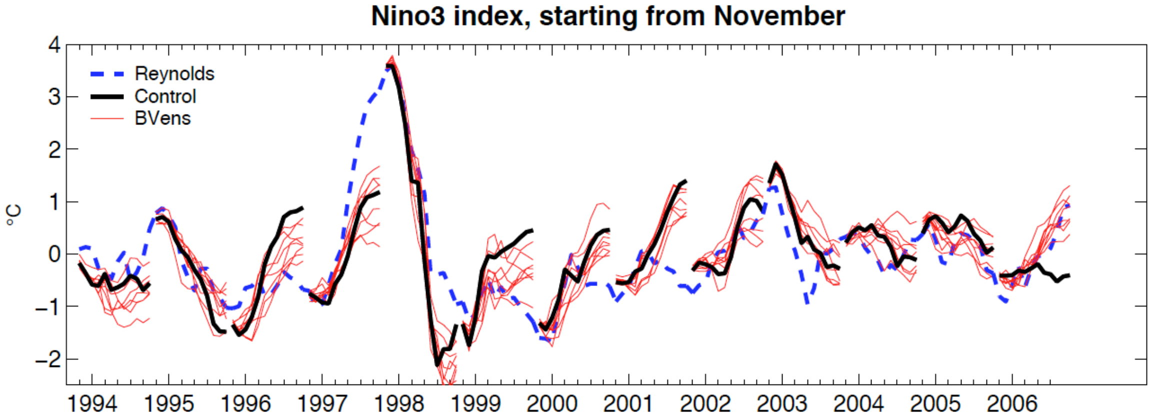

Figure 3 Niño3 index anomaly forecast starting from November initial conditions showing the ensemble perturbed with 4 pairs of BVs (red lines) the control forecast initialized with the unperturbed initial condition (black line). Results are validated with the observed Niño3 index (the Reynolds SST), denoted as the dashed blue line. The forecast anomalies are calculated relative to the climatological forecast drift.

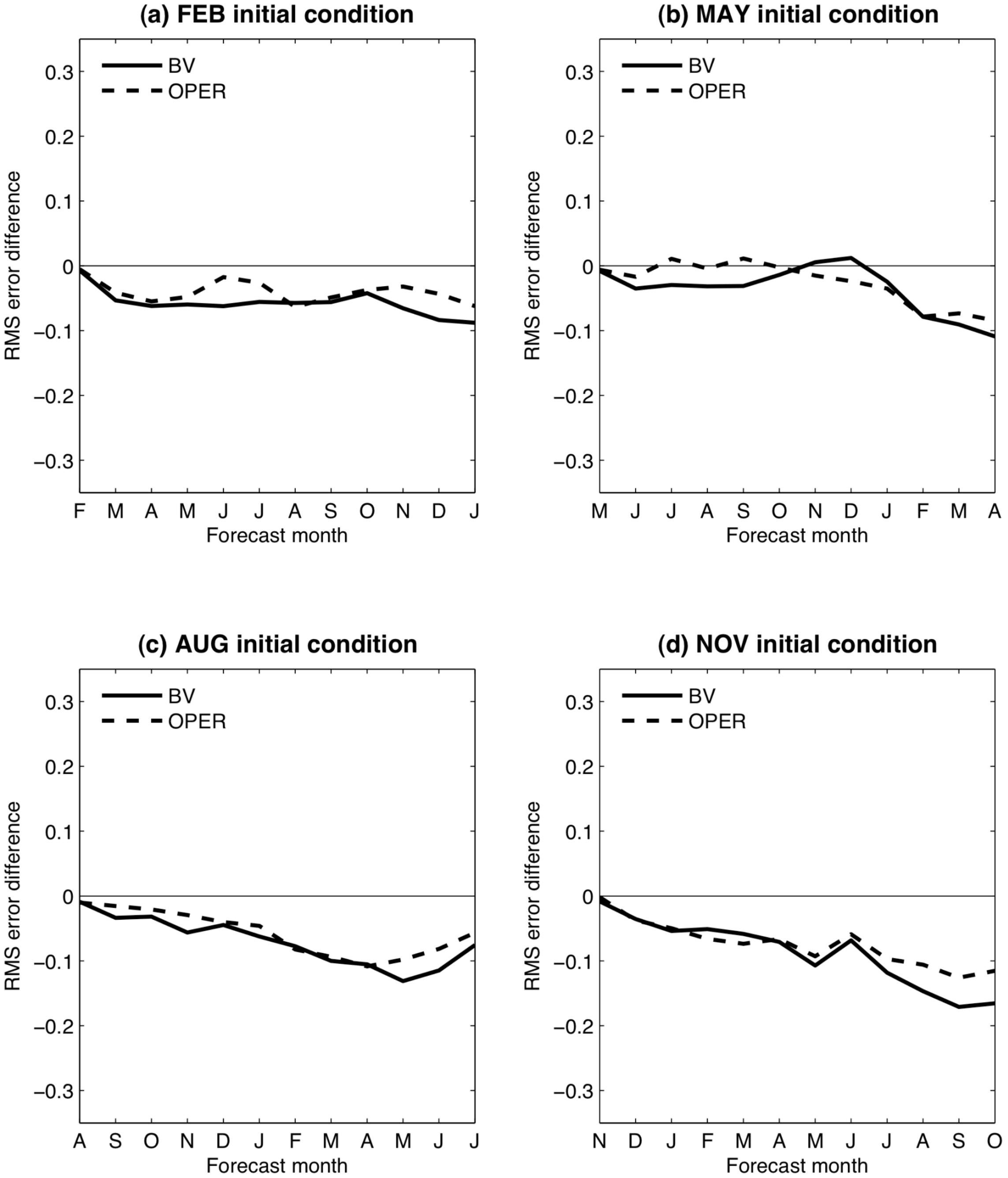

Figure 3 Differences in mean RMS error between the ensemble mean and the control forecasts with the BV and operational ensemble system for (a) February, (b) May, (c) August and (d) November initial conditions during the period of 1993 to 2005. The solid lines indicate the result from using the BV ensemble and the dashed lines for the operational ensemble. Mean RMS error is defined as the time-averaged RMS difference between the observed SST anomaly (Reynolds SST) and the forecast SST anomaly in the tropical central-eastern Pacific (180°-90°W, 15°S-15°N).

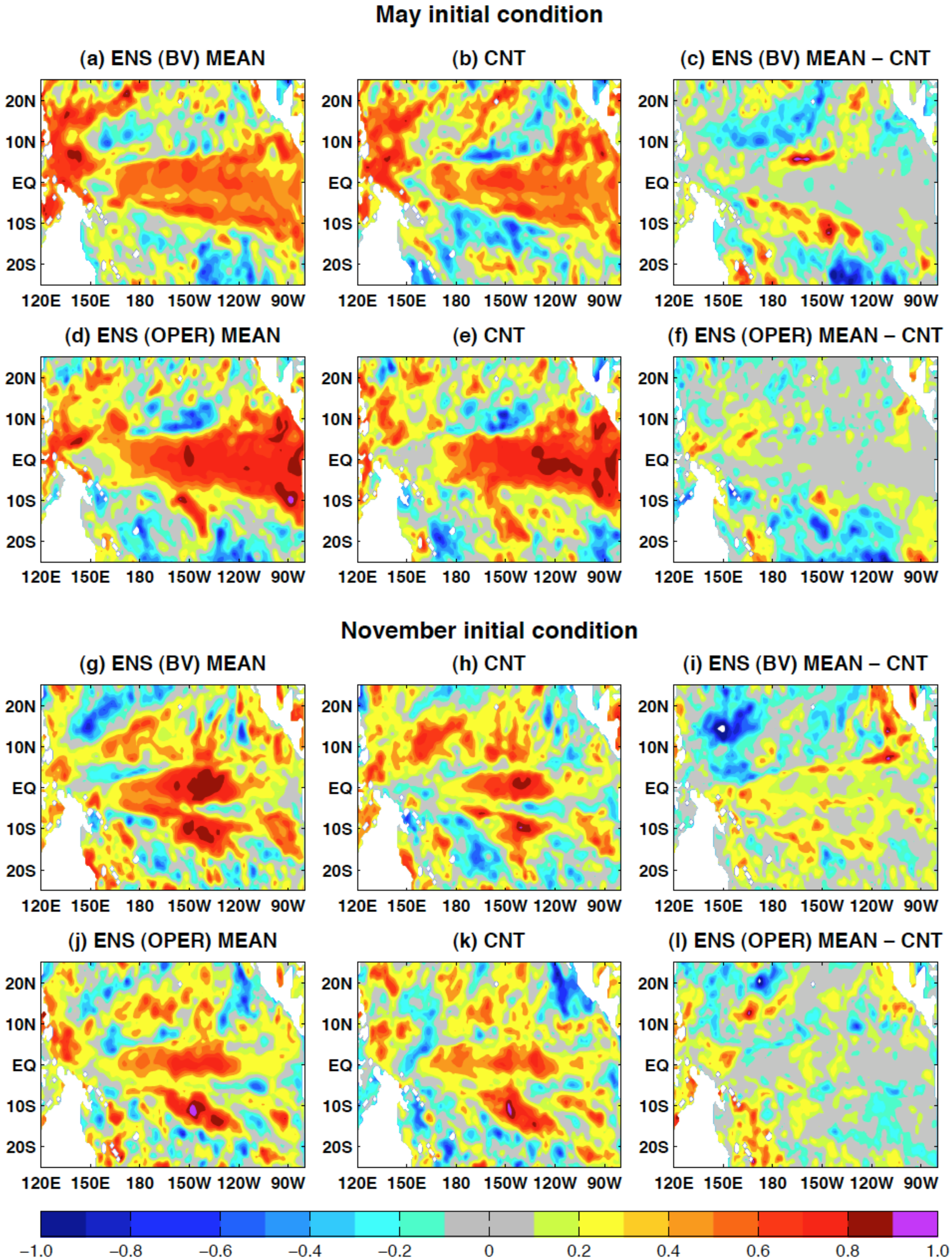

Figure 4 SST anomaly correlations with observations at the 9th-month lead time for mean ensemble-forecasts (left panels), unperturbed (control, middle panels) and the differences between the ensemble mean and unperturbed forecasts (right panels). (a)-(c) are for the BV ensemble system from May initial conditions. (d)-(f) are the same as (a)-(c) excpet for the operational ensemble system. (g)-(l) are the same as (a)-(c) expect from November initial conditions.

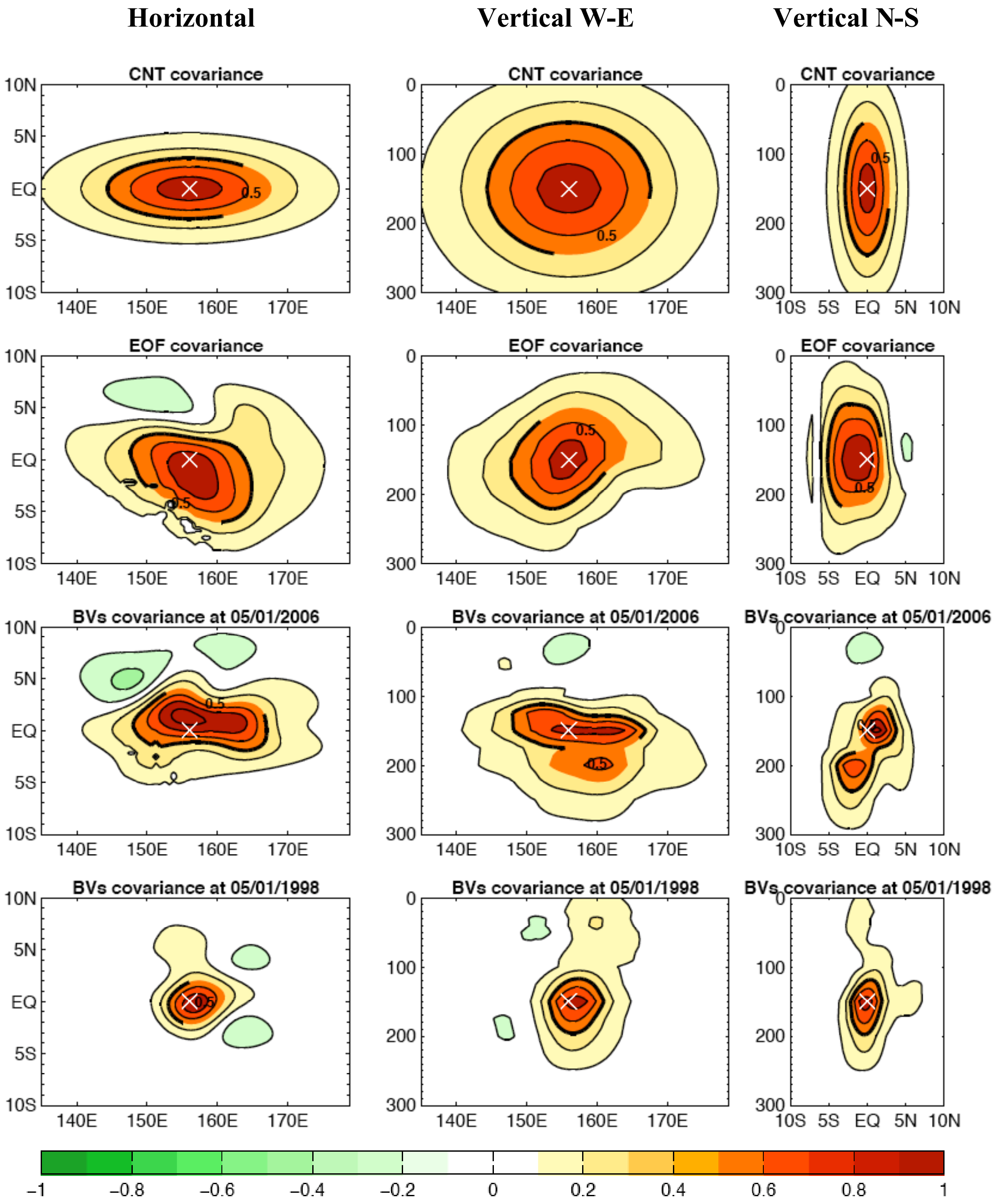

Figure 5 Temperature correlation structure associated with a hypothetical temperature observation at (156°E, Equator, 150m, denoted by ×) in the control (a Gaussian function, first row), the 4EOF-case (second row), the 4BV-case in May 2006 (third row) and the 4BV-case in May 1998 (fourth row). Horizontal, zonal and the meridional cross sections are shown from left to right, respectively.

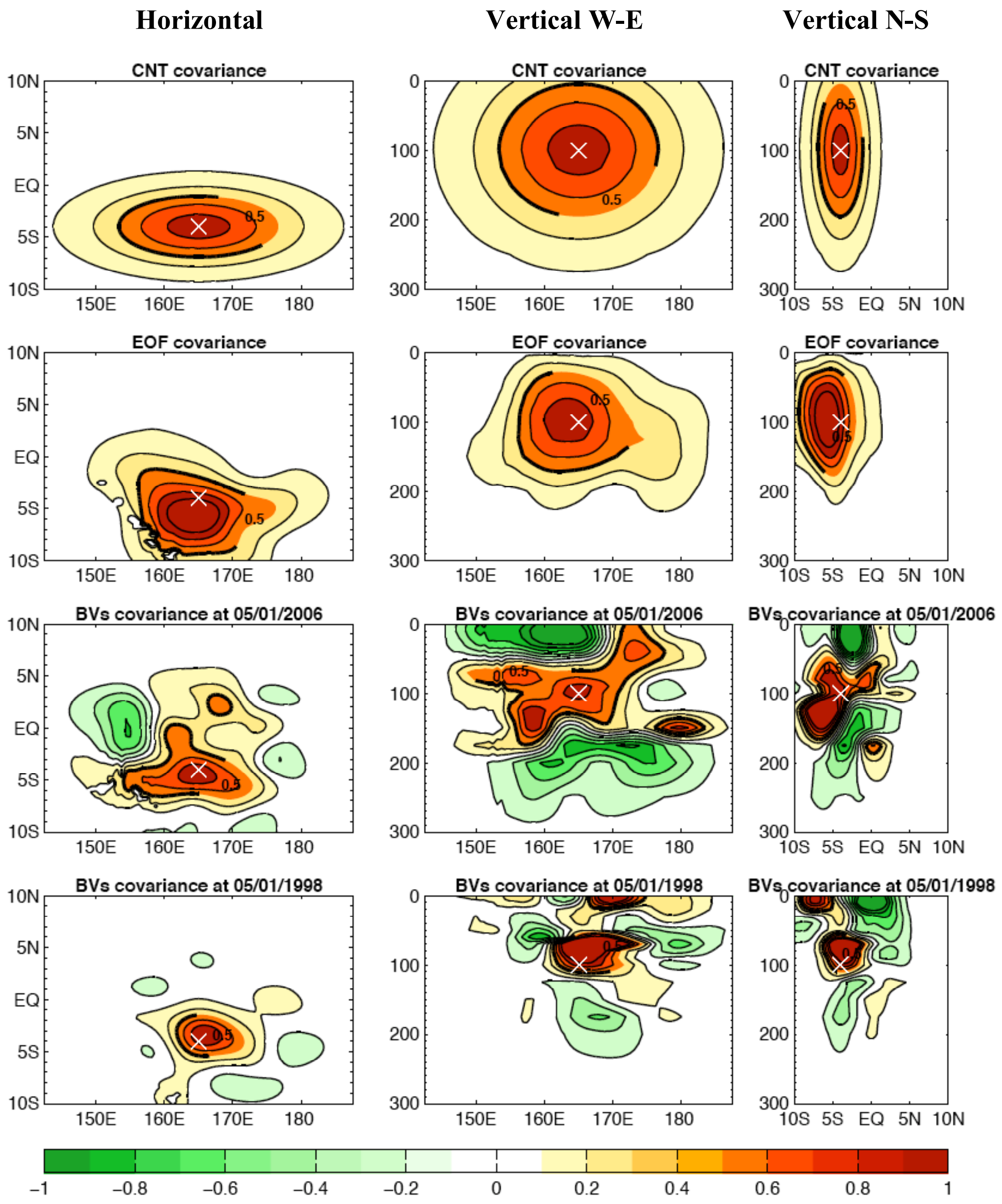

Figure 4 Same as Figure 5 but for a salinity observation at (165°E, 4°S, 150m).

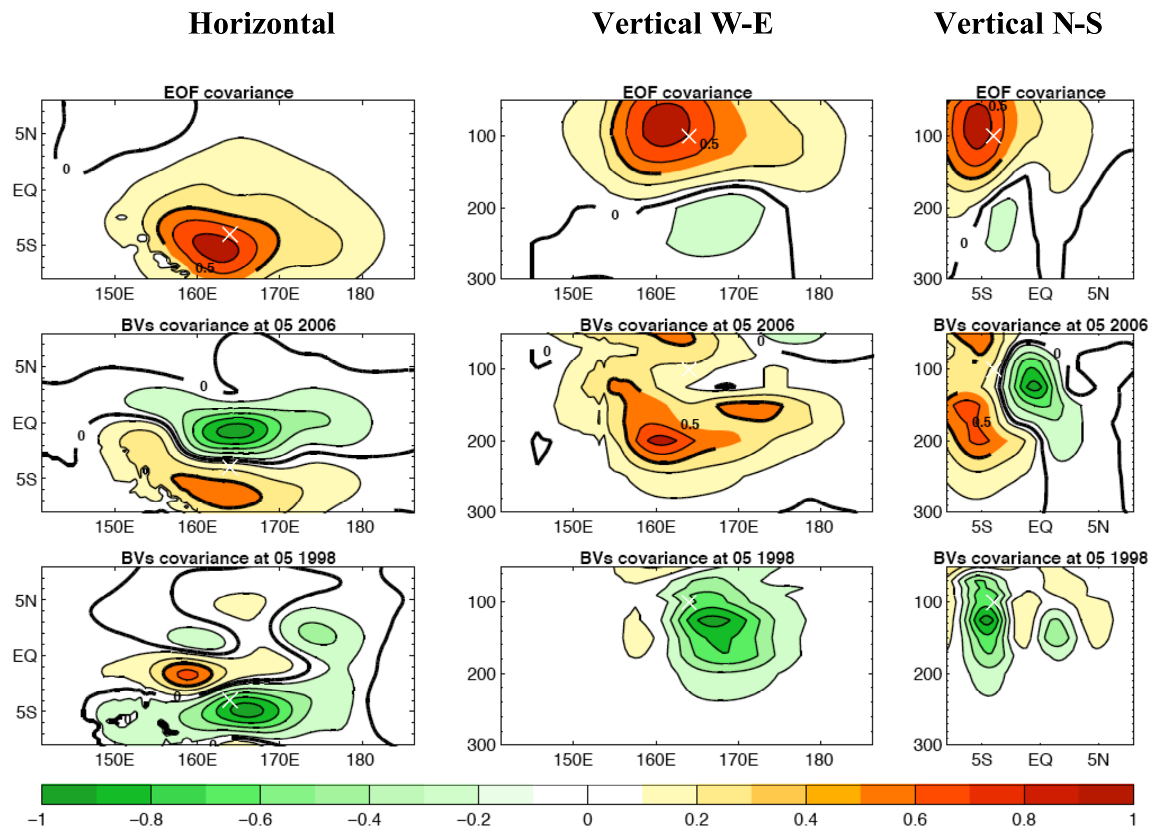

Figure 7 Temperature correlation structure associated with a hypothetical salinity observation at (165°E, 4°S, 100m, denoted by ×) in the 4EOF-case (first row), the 4BV-case in May 2006 (second row) and the 4BV-case in May 1998 (third row). Horizontal, zonal and the meridional cross sections are shown.

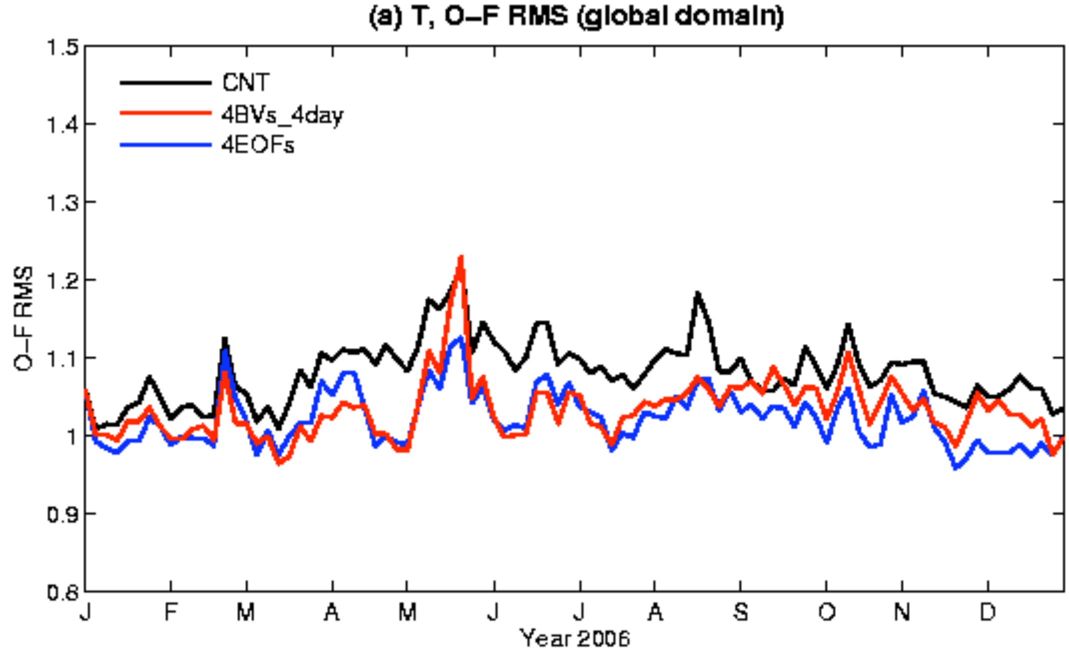

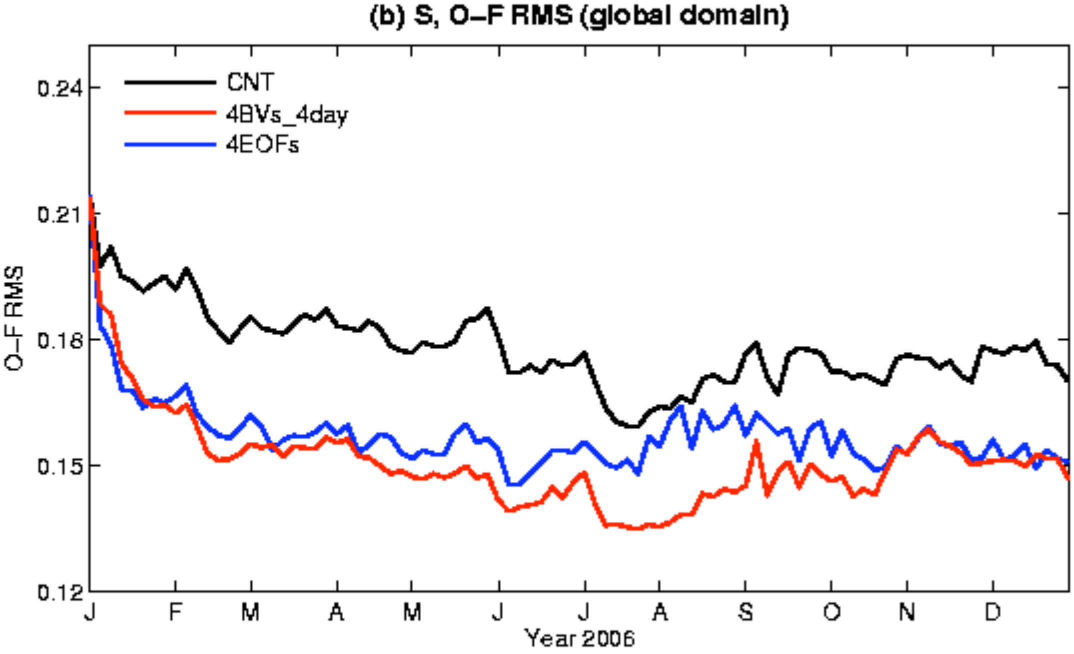

Figure 8 Time series of the global RMS of (a) the temperature OMF and (b) the salinity OMF.

(a) $\mathrm{OMF}_{\mathrm{CNT}} - \mathrm{OMF}_{\mathrm{4BV}}$

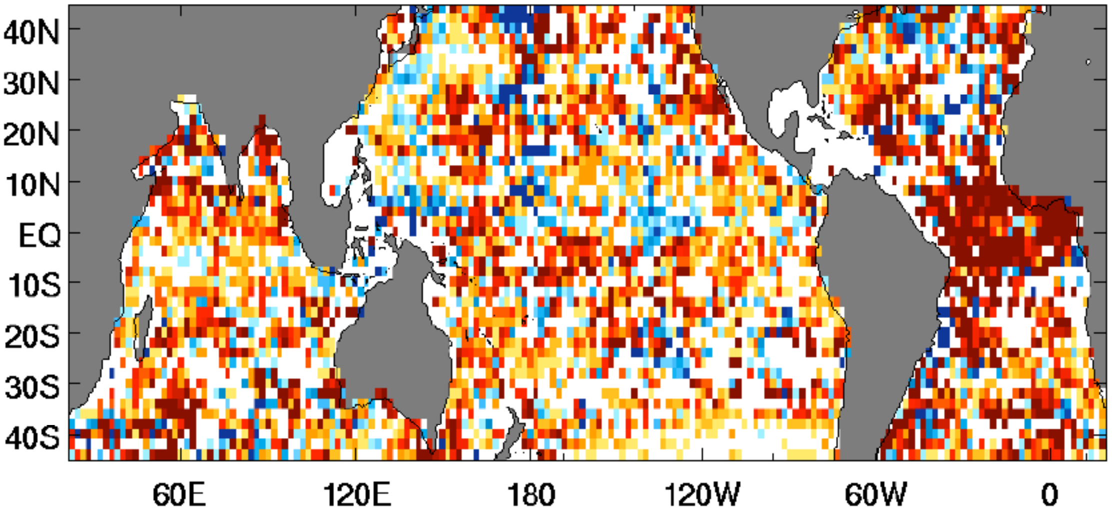

(b) $\mathrm{OMF}_{\mathrm{CNT}} - \mathrm{OMF}_{\mathrm{4EOF}}$

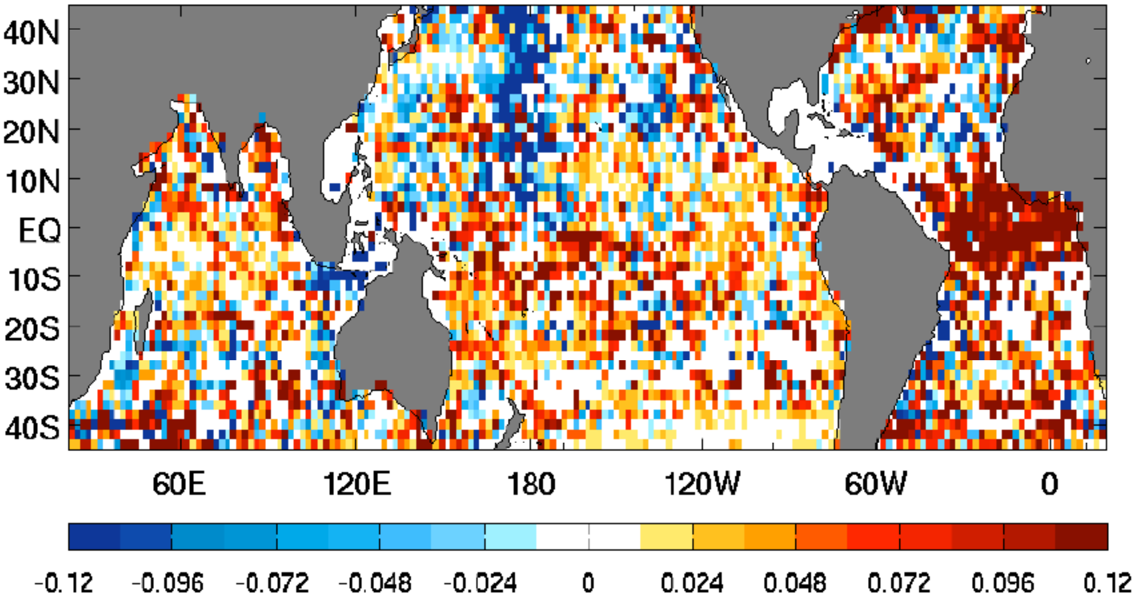

Figure 9 Differences between the salinity RMS OMF above 150m of the control and of (a) the 4BV analyses and (b) the 4EOF analyses.

(a) Pacific Ocean

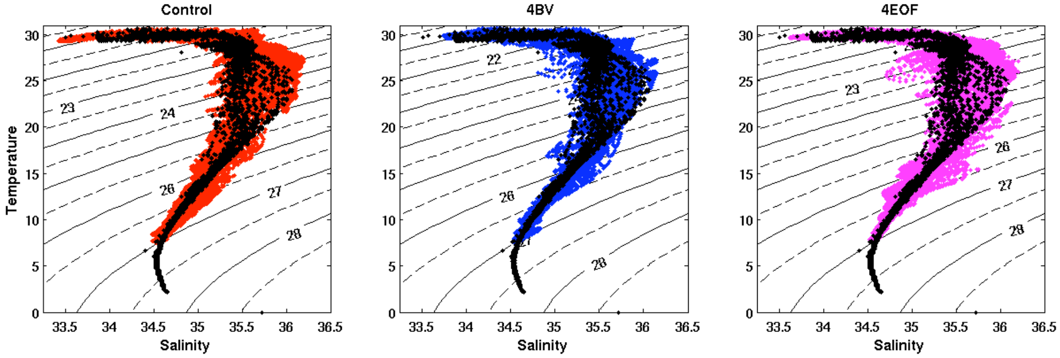

(b) Atlantic Ocean

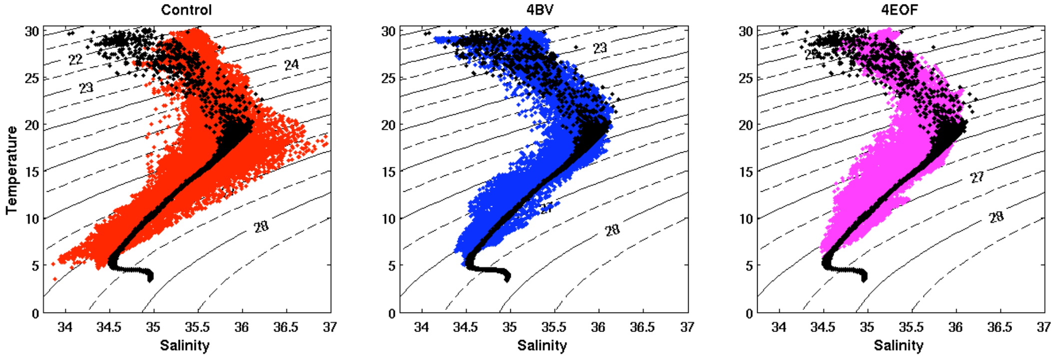

(c) Indian Ocean

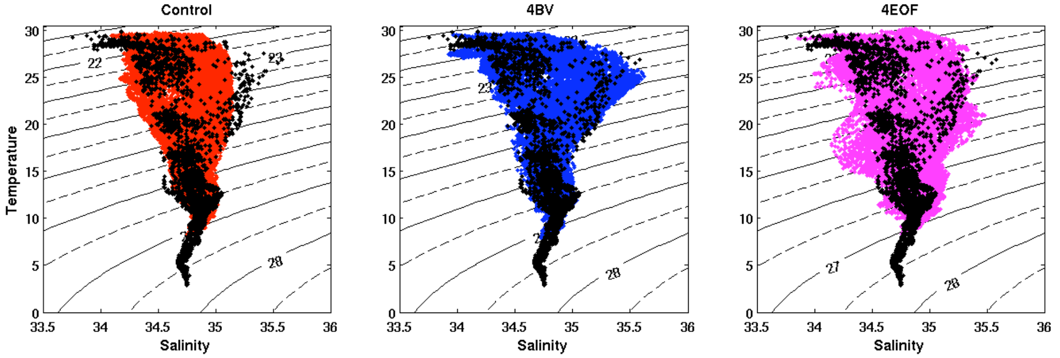

Figure 10 T-S-diagram from the analysis (colored dots) and the CTD data (black dots) in (a) the south western equatorial Pacific (162.5°E-167.5°E, 0°S-5°S), (b) the northern tropical Atlantic (2.5°W-2.5°E, 2°N-7°N) and (c) the south east tropical Indian Oceans (85°E-90°E, 4°S-9°S). Note that the contours are isolines of σ_θ.

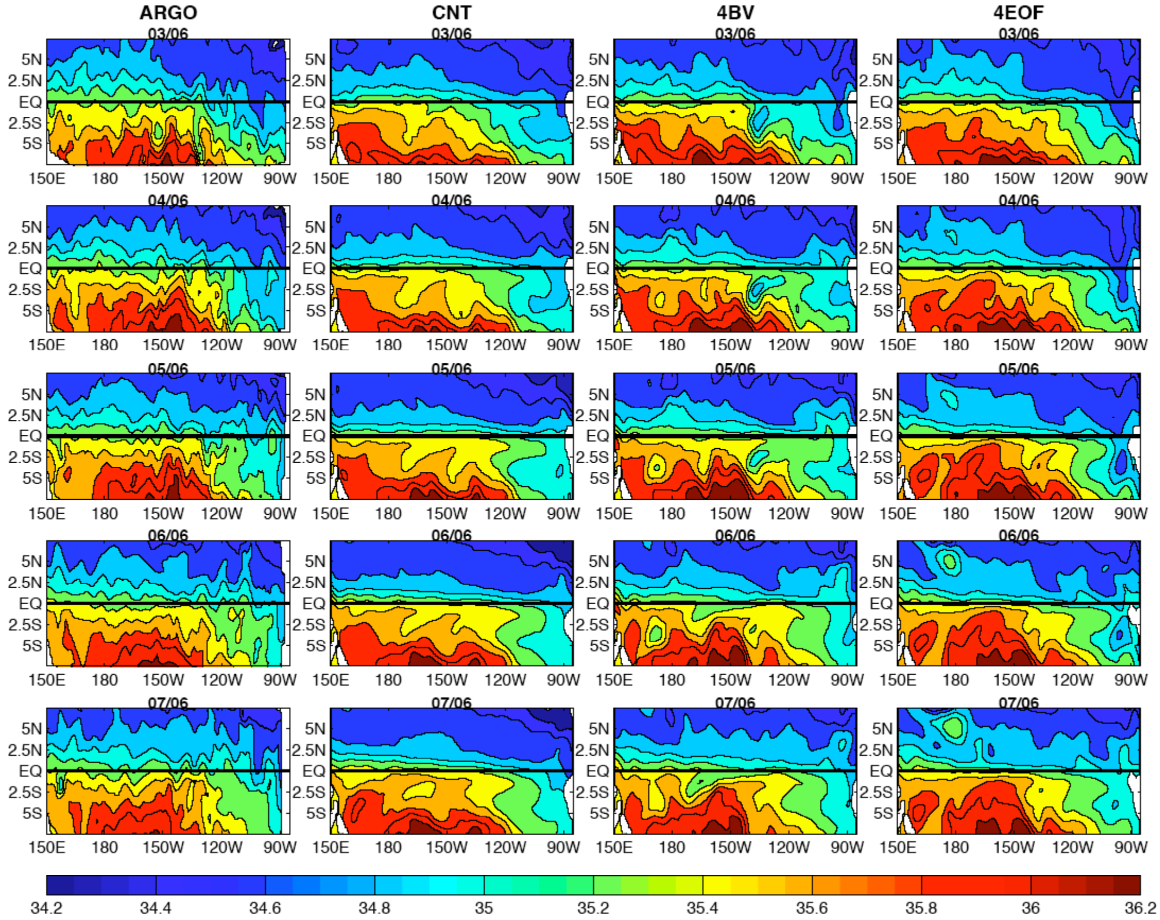

Figure 5 Monthly-mean salinity on the 24.5 kg m^{-3} density surface from March 2006 to July 2006. From left to right are the Argo data, the control analysis, the 4BV analysis and the 4EOF analysis. Each map uses the same 30 days of Argo salinity, from March through July 2006.

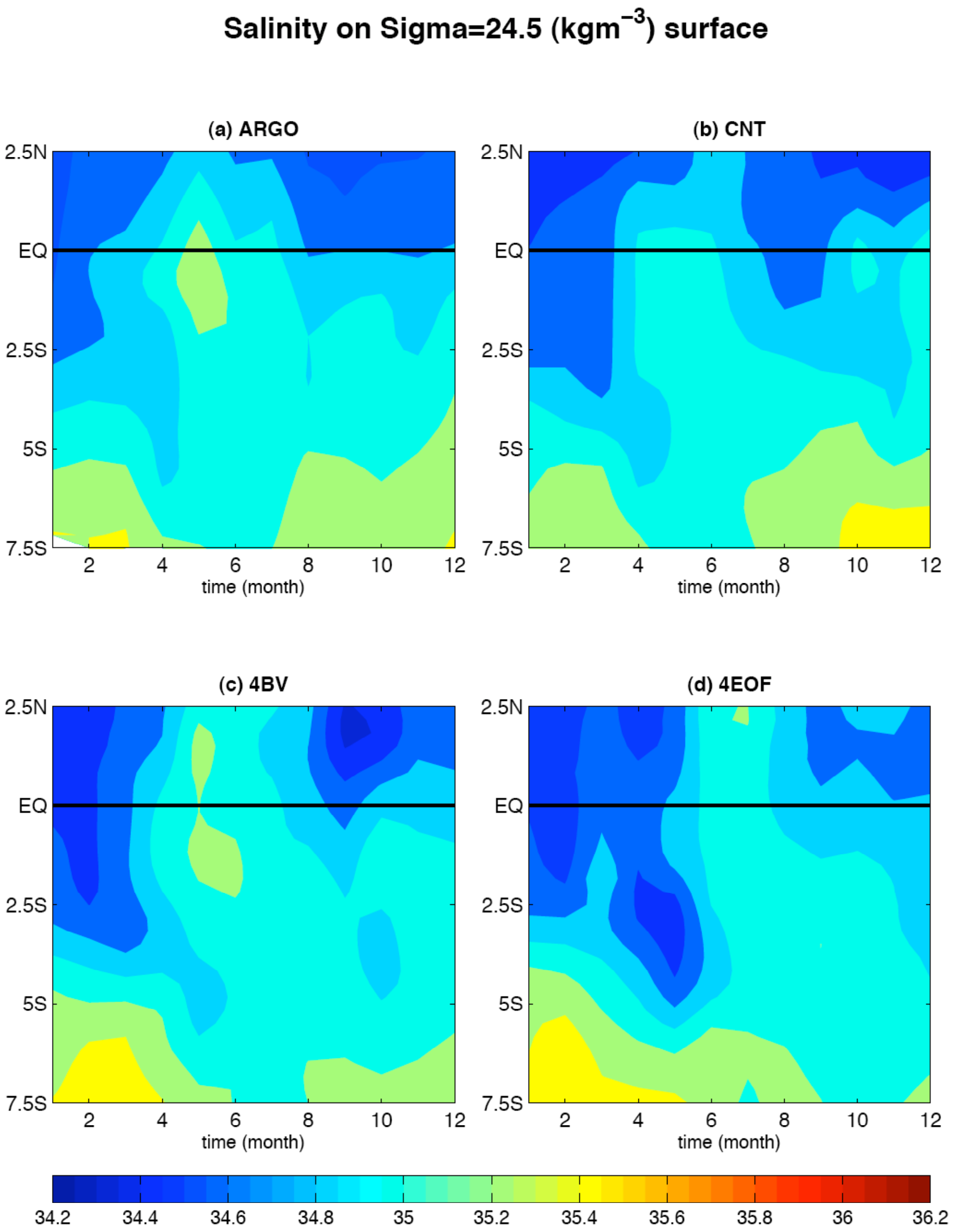

Figure 12 Salinity variations along a meridional cross-section at 93.5°W during 2006 in (a) the ARGO data, (b) the control analysis, (c) the 4BV analysis, and (d) the 4EOF analysis.